Hindawi
Shock and Vibration
Volume 2024, Article ID 2804173, 20 pages
https://doi.org/10.1155/2024/2804173

Research Article

A Novel Method for Identifying Resonance Frequency Band in Weak Bearing Fault Diagnosis of Electric Driving System

Cong Yue,[1] Yu Zhu,[1] Ping Cheng,[1] Bei Wang,[2] and Kai Wang[2]

[1]*Logistics Engineering College, Shanghai Maritime University, Shanghai 201306, China*
[2]*NIO, Shanghai, China*

Correspondence should be addressed to Cong Yue; yuecong234@163.com

Received 8 December 2023; Revised 18 February 2024; Accepted 22 February 2024; Published 6 March 2024

Academic Editor: Xian-Bo Wang

Because of the uncertainty of the structure and environment of the electric driving system (EDS), the fault signature of the rotating mechanism is complicated. A novel method based on Hilbert transform with modified fast kurtogram (HTMFK), which is used for identifying the bearing faults in the EDS, is proposed. The modified principle and algorithm flow of the proposed method are derived. A high pass filter based on the frequency band identified by HTMFK is constructed and applied to fault diagnosis. Simulation signals demonstrate the ability of demodulating signals and identifying the fault resonance band. The bearing fault bench experiment of EDS is carried out in a semianechoic chamber. The corresponding fault tests are conducted according to different operating conditions. The applicability of HTMFK is verified by comparing the square envelope spectrums. Compared with other methods, the proposed method identifies the fault resonance frequency band more effectively and expands the application range of bearing fault diagnosis in EDS.

1. Introduction

In recent years, electric vehicles have developed rapidly and gradually become one of the important directions for the development of automobiles. As a result, people are increasingly concerned about the quality and lifespan of electric vehicles. The electric driving system (EDS), as the power source of electric vehicles, has a significant impact on the reliability of vehicles quality. The rolling bearing is an important component of EDS, which usually operates in high-speed and high-pressure environments [1–3]. If there is a defect in a certain part of the rolling bearing during the operation process, the periodic impact caused by the defect will generate structural resonance of EDS. Therefore, monitoring the vibration information and extracting the impact in the signal can effectively diagnose whether there is a fault in the rolling bearing [4–6]. Furthermore, abnormal operating condition of EDS cannot be detected in time during the operation of an electric vehicle may cause incalculable structural damage, more serious even lead to safety accidents. As a result, efficient and accurate diagnosis of bearing fault in EDS has a high engineering application value.

Due to the interference from other rotating components in EDS and energy attenuation caused by transmission paths, the vibration response of rolling bearings often exhibits multicomponent and nonlinear characteristics, which results in weak fault characteristics in the signal [7]. In addition, fluctuations of rotational speed also lead to the phenomenon of nonstationary characteristics. In general, the vibration signal of fault rolling bearings has three main characteristics: interference of strong noise, nonlinearity, and nonstationarity [8]. Therefore, extracting the characteristics of bearing faults from signals accurately plays an important role in diagnosis analysis [9]. To address this issue, domestic and foreign scholars have proposed many effective methods.

Signal decomposition is one of the mainstream research directions. Fault features can be extracted from the signal components which contain fault information. Empirical mode decomposition (EMD) decomposes the signal adaptively and extracts different components from the signal

processing [10]. Combining with Hilbert transform, EMD is widely used in bearing fault analysis [11, 12]. Jia et al. [13] proposed a new method that combines the improved EMD with adaptive maximum second-order cyclostationarity blind deconvolution, which extracts the weak fault components of roller bearings effectively. Due to the deficiency of modal aliasing and endpoint effects in EMD, Wu and Huang [14] incorporated Gaussian white noise before using EMD and proposed ensemble empirical mode decomposition (EEMD). Nevertheless, illusive components of IMF may appear and the computational efficiency of EEMD is relatively low during the process of adding white noise by EEMD. To address this issue, scholars have proposed many improved algorithms, such as CEEMD [15] and MEEMD [16]. On the other hand, variable mode decomposition (VMD) can achieve effective separation of signal frequency domain adaptively, which can avoid the problem of modal aliasing [17, 18]. Gu et al. [19] proposed a method based on VMD and permutation entropy. Meanwhile, the effectiveness of features extracted by EMD, EEMD, and the proposed method was compared through support vector machine. However, the parameter settings of VMD can have a significant impact on the accuracy of its decomposition results. Regarding this issue, Jin et al. [20] optimized the grey wolf optimization algorithm (GWO) and applied it to the parameter optimization of VMD and deep belief networks (DBN). Besides, singular value decomposition (SVD) is a matrix factorization method which decomposes matrices into singular value matrices and unitary matrices. The product of different singular values and unitary matrices represents different components in the signal [21]. When dealing with certain weak faults, SVD may have difficulty to extract weak components from the signal. Therefore, Zhu et al. [22] proposed an improved SVD for extracting weak fault components and demonstrated the decomposition ability of SVD through Hankel matrix. EWT is also a method for signal decomposition, which decomposes a signal into components of different frequency bands by setting multiple filters [23]. The shortcoming of initial EWT is that unreasonable frequency band division occurs when deals with certain weak faults signals. Therefore, many scholars have made improvements to avoid this problem [24, 25]. However, one shortage of EWT is the lack of an indicator to determine the frequency band of fault components adaptively.

Determining the resonance frequency band of the fault impulse component can also assist the extracting fault components and features. The kurtosis value of a time-domain signal is a commonly indicator which reflects the magnitude of the fault impact [26]. Dwyer [27] proposed the concept of spectral kurtosis (SK), which extends time-domain kurtosis to the frequency function. However, because of the lack of a formal definition and computational complexity of SK, it has not been fully applied in the field of engineering application. Antoni and Randall [28–30] provided a detailed definition and theoretical basis for SK, and proposed a fast calculation method called Fast Kurtogram (FK) by binary trees. Although FK can adaptively select the resonance frequency band of the fault component, the problem of frequency band division being fixed and kurtosis indicator being ineffective for certain weak faults still exists. Therefore, many researchers have made improvements and evolve many variants of FK to address this issue [31–34]. Song et al. [35] used balanced envelope and Protrugram, which is a variant of kurtogram, to achieve automatic fault diagnosis with solving the problem of information loss caused by variable speed. Chen et al. [36] proposed the concept of envelope spectrum family for optimizing envelope spectrum and combined the optimal envelope spectrum with the proposed new indicator to propose the product envelope spectrum optimization graph (PESOgram). In addition, the robustness of this method was verified by comparing different methods. Meng et al. [37] utilized weighted empirical mode decomposition and Infogram for envelope analysis, which was verified by experiments and comparisons to detect more accurate initial fault times. Li et al. [38] proposed Cyclogram based on cyclostationarity and kurtosis. The effectiveness of Cyclogram was verified through simulation and real signals.

However, the improved FK methods may also fail in some cases of weak faults, because of the inaccuracy identification of resonance frequency band of the faulty component. In this paper, a fault diagnosis method of Hilbert transform with modified fast kurtogram (HTMFK) for bearing weak fault feature identification is proposed while consider the rotating machinery operation characteristics of EDS. The feasibility is verified through simulation experiments. To verify the practicality of proposed method, the rolling bearing fault bench tests of EDS is designed and implemented. The resonance frequency of the outer ring fault of rolling bearing is detected by HTMFK. The precision of the resonance frequency band discriminated is verified through variable speed experimental data. A high pass filter (HPF) is designed based on the determined resonance frequency band under different steady operating modes for identifying the fault. The results indicate that the proposed method can be used for fault diagnosis of bearing fault in EDS with higher accuracy and scope of application than FK and the other compared method.

2. Theory and Derivation

Due to the complex of the vibration transmission path, the fault signal in EDS becomes weak and difficult to extract. This section introduces the basic theory of HTMFK. The improved processing is put forward to obtain a new signal with amplified fault information. Finally, the resonance frequency band is obtained by FK on the processed signal.

2.1. Hilbert Transform Theory. The Hilbert transform calculates the imaginary part of signal $a(t)$ by convolving $a(t)$ and $1/\pi t$. This method converts the signal from the plane to the Hilbert space, obtaining a complete analytical signal.

$$H[a(t)] = \frac{1}{\pi}\int_{-\infty}^{+\infty}\frac{a(t)}{t-\tau}\mathrm{d}\tau, \tag{1}$$

where $H[a(t)]$ represents signal $a(t)$ to perform Hilbert transform. From this, the analytical signal $h(t)$ can be obtained as follows:

$$h(t) = a(t) + j \cdot H[a(t)]. \tag{2}$$

After obtaining the analytical signal $h(t)$, the instantaneous amplitude and phase of $a(t)$ can be calculated to prepare for subsequent signal processing. The calculation formula for instantaneous amplitude is as follows:

$$A[a(t)] = \sqrt[2]{[a(t)]^2 + \{H[a(t)]\}^2}, \tag{3}$$

where $A[a(t)]$ represents the calculation of instantaneous amplitude of $a(t)$.

The instantaneous phase $a(t)$ can be calculated as the following formula:

$$\varphi(t) = \arctan \frac{H[a(t)]}{a(t)}, \tag{4}$$

where $\varphi(t)$ represents the instantaneous phase of $a(t)$.

Through the Hilbert transform, the Hilbert envelope is calculated and provides theoretical support for subsequent signal improvement processing.

2.2. Spectral Kurtosis Theory. Kurtosis is a fourth order statistic and is suitable for detecting shocks in a signal. The basic calculation formula for discrete signal is as follows:

$$K = \frac{1}{N} \sum_{i=1}^{N} \left(\frac{x_i - \overline{x}}{\sigma_t} \right)^4, \tag{5}$$

where σ_t is the standard deviation of discrete signal x_n.

Spectral kurtosis refers to the kurtosis value of the components of a signal at different frequencies. By performing Wold–Cramér decomposition on a nonstationary random signal $x(t)$ with zero mean, it can be expressed as follows:

$$x(t) = \int_{-1/2}^{+1/2} H(t, f) e^{j2\pi ft} \mathrm{d}Z_x(f), \tag{6}$$

where $Z_x(f)$ is the spectral process of white noise and $H(t, f)$ is the complex envelope of $x(t)$ at frequency f. $H(t, f)$ can be represented by the following formula:

$$H(t, f) = \int_{-\infty}^{+\infty} [x(\tau)\omega(\tau - t)] e^{-j2\pi ft} \mathrm{d}\tau. \tag{7}$$

Signal $x(t)$ by spectral kurtosis can define as a fourth order normalized cumulant as follows:

$$\begin{aligned} K_x(f) &= \frac{S_{4x}(f) - 2S_{2x}^2(f)}{S_{2x}^2(f)} \\ &= \frac{S_{4x}(f)}{S_{2x}^2(f)} - 2, \end{aligned} \tag{8}$$

where $S_{4x}(f)$ and $2S_{2x}^2(f)$ are the fourth and second moments of complex envelope $H(t, f)$, respectively. In addition, the rotating machinery always contains a stationary random noise $c(t)$, so that the spectral kurtosis $K_{x+c}(f)$ of nonstationary random signal $x(t)$ containing noise can also be expressed as follows:

$$K_{x+c}(f) = \frac{K_x(f)}{[1 + \rho(f)]^2}, \tag{9}$$

where $\rho(f)$ indicates signal-to-noise ratio.

The spectral kurtosis theory provides theoretical support for FK. Based on the above theory and signal process processing, the HTMFK can be derived.

2.3. Principal Derivation of HTMFK. The fault signal $y(t)$ is composed of fault information $x(t)$ and noise $c(t)$ superimposed together, which is shown in the following form:

$$y(t) = x(t) + c(t), \tag{10}$$

where $y(t), x(t), c(t)$ are time-domain signals. For weak faults impact, the energy of fault signature is usually smaller than that of noise information. The amplitude of the signal is demodulated by Hilbert envelope to reduce noise and increase fault information. The expression of processed signal $g(t)$ is as follows.

$$\begin{aligned} g(t) &= \frac{y(t)}{A[y(t)]} \\ &= \frac{x(t) + c(t)}{A[y(t)]} \\ &= \frac{x(t) + c(t)}{\sqrt[2]{[y(t)]^2 + \{H[y(t)]\}^2}}. \end{aligned} \tag{11}$$

During the sampling and calculation process, the signals $y(t), x(t), c(t), g(t)$ are discretized and a matrix composed of column vectors can be obtained.

$$\begin{bmatrix} y_n \\ x_n \\ c_n \\ g_n \end{bmatrix}^T = \begin{bmatrix} y_1 & y_2 & \cdots & y_n \\ x_1 & x_2 & \cdots & x_n \\ c_1 & c_2 & \cdots & c_n \\ g_1 & g_2 & \cdots & g_n \end{bmatrix}^T. \tag{12}$$

The discrete form of equation (10) is as follows:

$$\begin{bmatrix} y_1 \\ y_2 \\ \vdots \\ y_n \end{bmatrix} = \begin{bmatrix} x_1 \\ x_2 \\ \vdots \\ x_n \end{bmatrix} + \begin{bmatrix} c_1 \\ c_2 \\ \vdots \\ c_n \end{bmatrix}. \tag{13}$$

The discrete form of signal $g(t)$ with improved processing is as follows:

$$[\,g_1 \;\; g_2 \;\; \cdots \;\; g_n\,]^T = \left[\frac{x_1+c_1}{A[y_1]} \;\; \frac{x_2+c_2}{A[y_2]} \;\; \cdots \;\; \frac{x_n+c_n}{A[y_n]}\right]^T \; i = 1,\, 2,\, 3 \ldots\ldots n, \tag{14}$$

where $A[y_i]$ is the instantaneous amplitude of the discrete signal at point i.

The impact signal in the resonance frequency range will be amplified by the demodulated signal. The resonance frequency band of the demodulated signal is identified by FK, which improves the accuracy in identifying the resonance frequency band of the original signal. Finally, the square envelope spectrum (SES) of the filtered signal is calculated to achieve the diagnosis of weak faults in rolling bearings. The procedure of HTMFK algorithm is shown in Figure 1.

3. Simulation Experiment

In this section, three simulation experiments of sweep frequency signal, bearing fault signal without noise, and bearing fault signal with noise are put forward to verify the fault feature identification of HTMFK.

3.1. The Influence of Improved Processing Method on AM Sweep Signal. To explain the effect of the processing method, a simulated sweep signal with linear sweep signal and amplitude modulated (AM) signal is constructed. The linear sweep signal $f(t)$ is as follows:

$$f(t) = e^{j2\pi\left(f_0 t + 1/2kt^2\right)}, \tag{15}$$

where f_0 is the initial frequency and k is the frequency modulation. The expression of k is shown as follows:

$$k = \frac{f - f_0}{T}, \tag{16}$$

where f is the cutoff sweep frequency and T is the total sweep duration of t. According to equation (16), the expression for the amplitude modulation signal is as follows:

$$f_h(t) = \frac{t}{T} \cdot e^{j2\pi\left(f_0 t + 1/2kt^2\right)}. \tag{17}$$

The sweep duration is set to 3 s, with a sweep cutoff frequency of 25 Hz. The temporal waveform and frequency spectrum of the sweep signal are shown in Figures 2(a) and 2(b).

As shown in Figures 2(c) and 2(d), AM frequency signal is a linear modulation, and the energy distribution of the spectrum changes. HTMFK restores the AM sweep signal, and transforms the original signal. The time-domain diagram of the demodulated signal is shown in Figure 3, in which the HTMFK method can basically eliminate the influence of amplitude modulation from endpoint effects.

3.2. The Outer Ring Fault Simulation of Rolling Bearing. As the simulation results in Section 3.1, the HTMFK method can demodulate and normalize the AM signal. The resonance excited by rolling bearing faults rapidly decay because of the damping of the structural system. The bearing information is also affected by noise, which leads to difficulty in obtaining fault features. The next simulation signal $u(t)$ for the outer ring fault of a single impact rolling bearing is as follows:

$$u(t) = Ae^{-2\pi f_n t\xi} \sin\left(2\pi f_n \sqrt{1-\xi^2}\, t\right), \tag{18}$$

where A stands the amplitude, f_n is the resonance frequency caused by the fault impact, f_s is sampling frequency, f_o is outer ring fault frequency, and ξ is the damping coefficient. The parameters set for this simulation are shown in Table 1.

The simulation process and the results are shown in Figure 4. In Figure 4(d), the demodulated signal spectrum has more concentrated energy. The results indicate that the proposed method improve the accuracy and precision of FK in identifying resonance frequency bands efficaciously.

As equation (10), the signal contains noise components. Therefore, noise should be added to the simulation signal in Figure 4(a) and the signal in the first 1 second is extracted. The time-domain and spectrum diagrams of the simulation signal with noise are shown in Figure 5. From Figure 5(a), the impact in the simulation signal is drowned out by added noise and the kurtosis value of the time-domain signal is small. In Figure 5(b), the resonance frequency peak of the original signal is covered by the noise energy, and only the resonance peak around 3000 Hz is obvious. From Figure 5(c), the amplitude of the characteristic frequency of the outer ring fault (BPFO) is obscured by noise, which makes it difficult to determine the fault from the envelope spectrum. FK, HTMFK, Protrugram, and SVD are used for this simulation signal respectively, and the results are shown in Figure 6.

From Figures 6(a) and 6(b), HTMFK is more accurate to locate the resonance frequency band rather than FK. The center frequency (f_c) of the resonance frequency band located by HTMFK is around 3000 Hz, which has a smaller bandwidth (B_w). The phenomenon of concentrated spectral energy is similar with the demodulated signal in Figure 4(d). As shown in the Figures 6(c) and 6(d), Protrugram identifies f_c at 3100 Hz and SVD extracted the resonance region near 3000 Hz.

From Figure 7, bandpass filtering of resonance frequency band is performed for Figures 6(a)–6(c). The square envelope spectrum (SES) of the filtered signal is calculated. From the results of SES, the amplitude of HTMFK is more prominent at 100 Hz than FK, which is consistent with the theoretical fault characteristic frequency. Due to the larger B_w, the SES of Protrugram has more harmonic components at 100 Hz and the diagnostic results are relatively accurate. SVD has the best noise reduction effect while extracting the fault resonance region of SVD in correct. From Figure 8, the SES of IMF3 obtained by EEMD shows obvious fault characteristics, which has significant amplitudes at 100 Hz

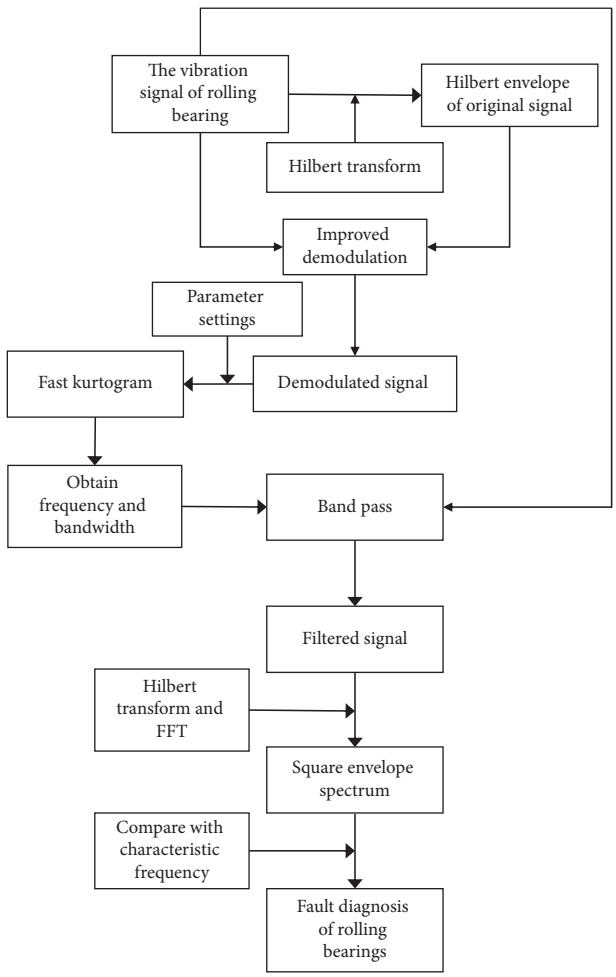

Figure 1: Flowchart of HTMFK algorithm.

and its harmonics. By comparing the results of 5 methods, all other methods except FK have good diagnostic performance.

4. Bench Test System of EDS

To verify the effectiveness of the proposed method for weak fault feature identification, a bench experiment of bearing fault in EDS is carried out. This section introduces the test system composition and operation conditions.

Faulty rolling bearing is conducted on a certain type of electric drive assembly under laboratory bench conditions. The position of the rolling bearing is at the output end of the motor shaft. The outer ring damage is caused by manual injury with a width of 0.6 mm and a depth of 0.03 mm, which is shown in Figure 9. The rolling bearing type is 6307 and the bearing parameters are shown in Table 2.

The operating conditions of the speed and motor torque for bench experiment are shown in Table 3. The experiment data are obtained by a high-precision data acquisition system. The signal sampling rate is set to 20 kHz. The sensor type is an IEPE acceleration sensor with a range of ±50 g. The sensor layout and experimental diagram are shown in Figure 10.

5. Fault Diagnosis and Validation

In this section, the applicability of the proposed method for fault identification is verified by several steady-state conditions. In addition, the effect of resonant fault band identification under variable speed condition is also used to verify the antidisturbance capability of the HTMFK.

5.1. Applicability Verification of HTMFK. The time domain and spectrum diagrams under the operating condition of 2000 rpm & 50 N·m are shown in Figure 11. The fault impact is obscured by noise and the kurtosis value is small. The spectrum in Figure 11(b) shows significant amplitudes around 3000 Hz and 6000 Hz. From Figure 11(c), the fault characteristics are completely obscured by noise and require further processing to extract fault features.

Different methods are used to process the experimental signals and the processing results are shown in Figure 12. From Figures 12(a) and 12(b), FK locates the resonance frequency range at a low frequency range below 1000 Hz while HTMFK locates at a high frequency range above 7000 Hz. From Figure 12(c), Protrugram determined f_c at 1150 Hz, which is similar to the FK result. Meanwhile,

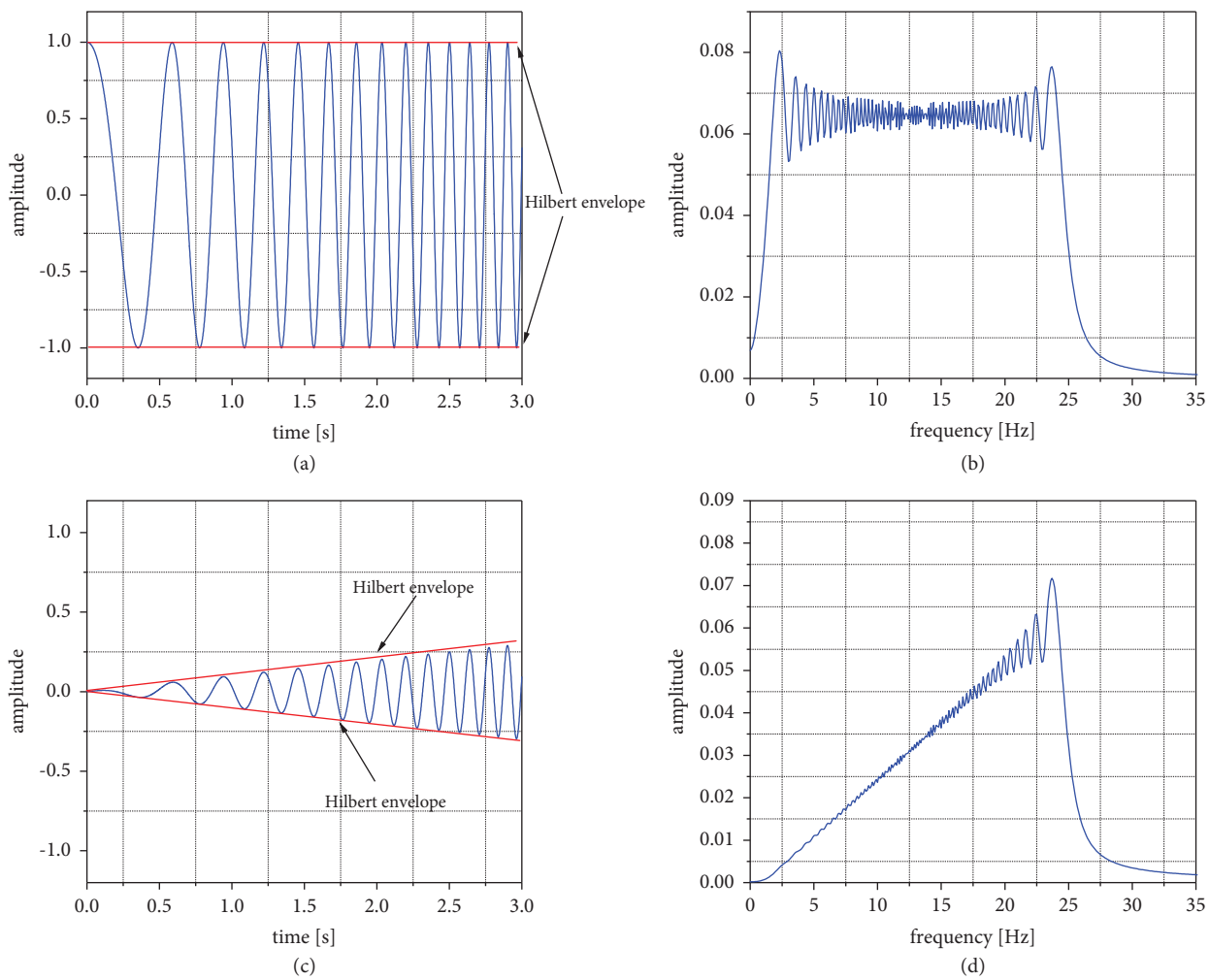

Figure 2: Schematic diagram of simulation sweep signal curve. (a) Temporal waveform of sweep signal. (b) Spectrum of sweep signal. (c) Temporal waveform of AM signal. (d) Spectrum of AM signal.

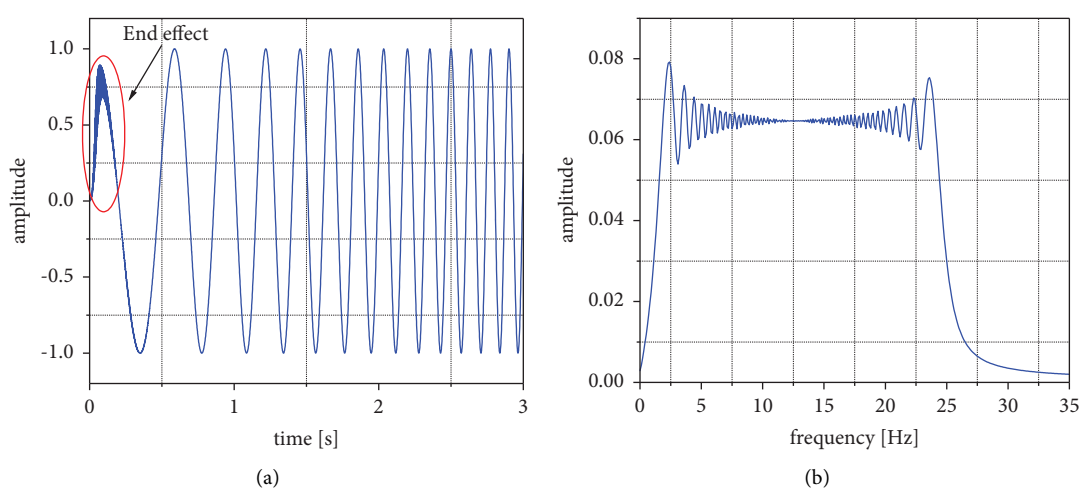

Figure 3: Improved processing of the AM sweeping signal. (a) Temporal waveform. (b) Spectrum.

Table 1: Parameters of simulation signals for outer ring faults.

A	f_s (Hz)	f_n (Hz)	ξ	f_o (Hz)
5	20000	3000	0.1	100

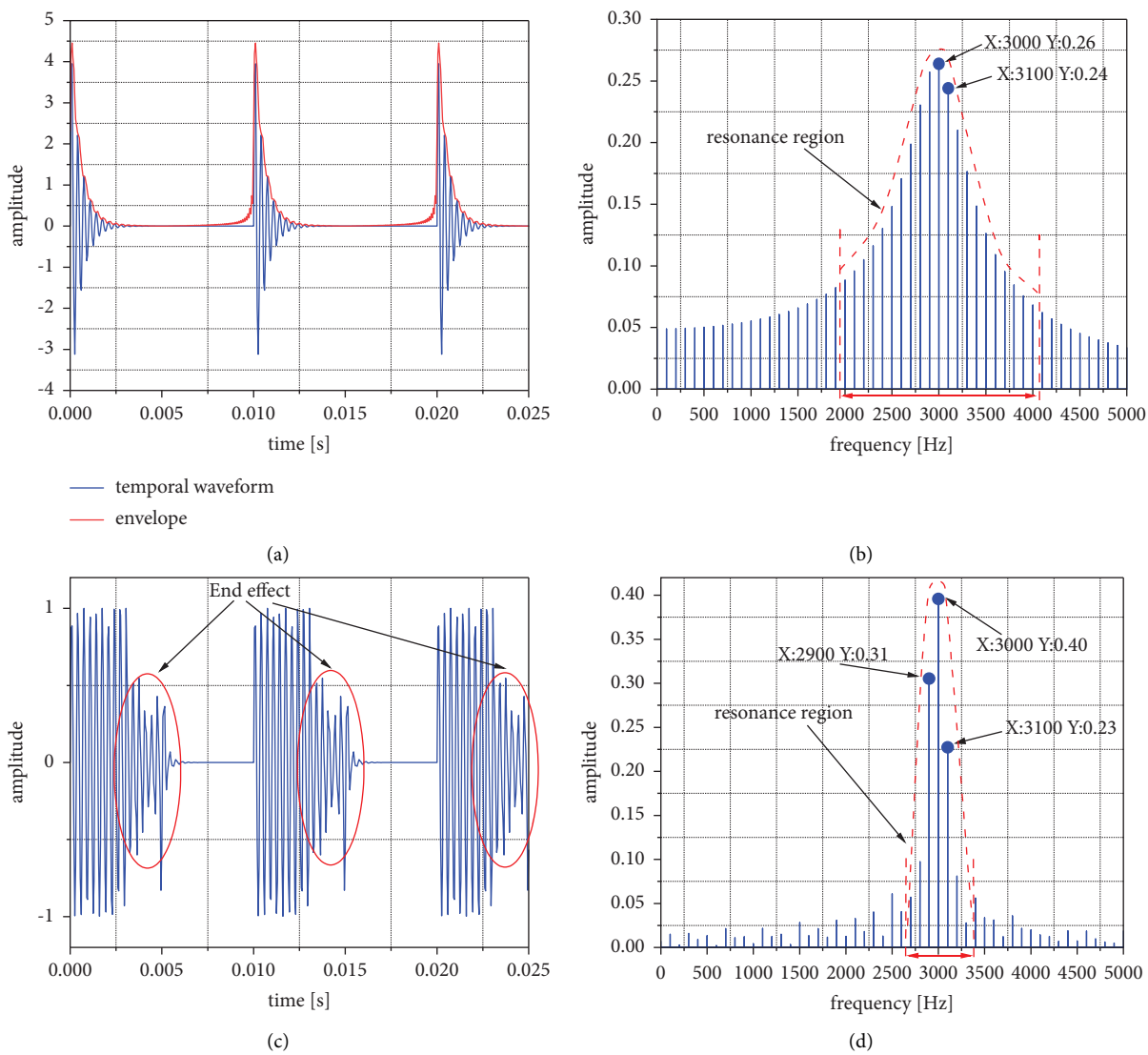

Figure 4: The simulation of outer ring fault without noise. (a) Initial impulse signal. (b) Spectrum of initial signal. (c) Processed simulation signal. (d) Spectrum of demodulated signals.

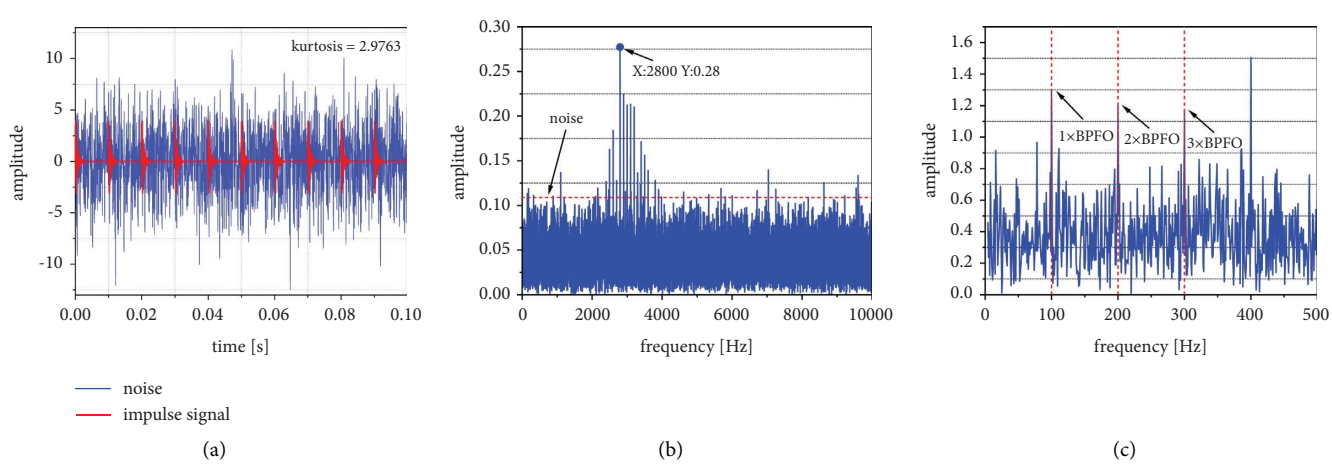

Figure 5: The simulation of outer ring fault with noise. (a) Temporal waveform. (b) Spectrum. (c) Envelope spectrum.

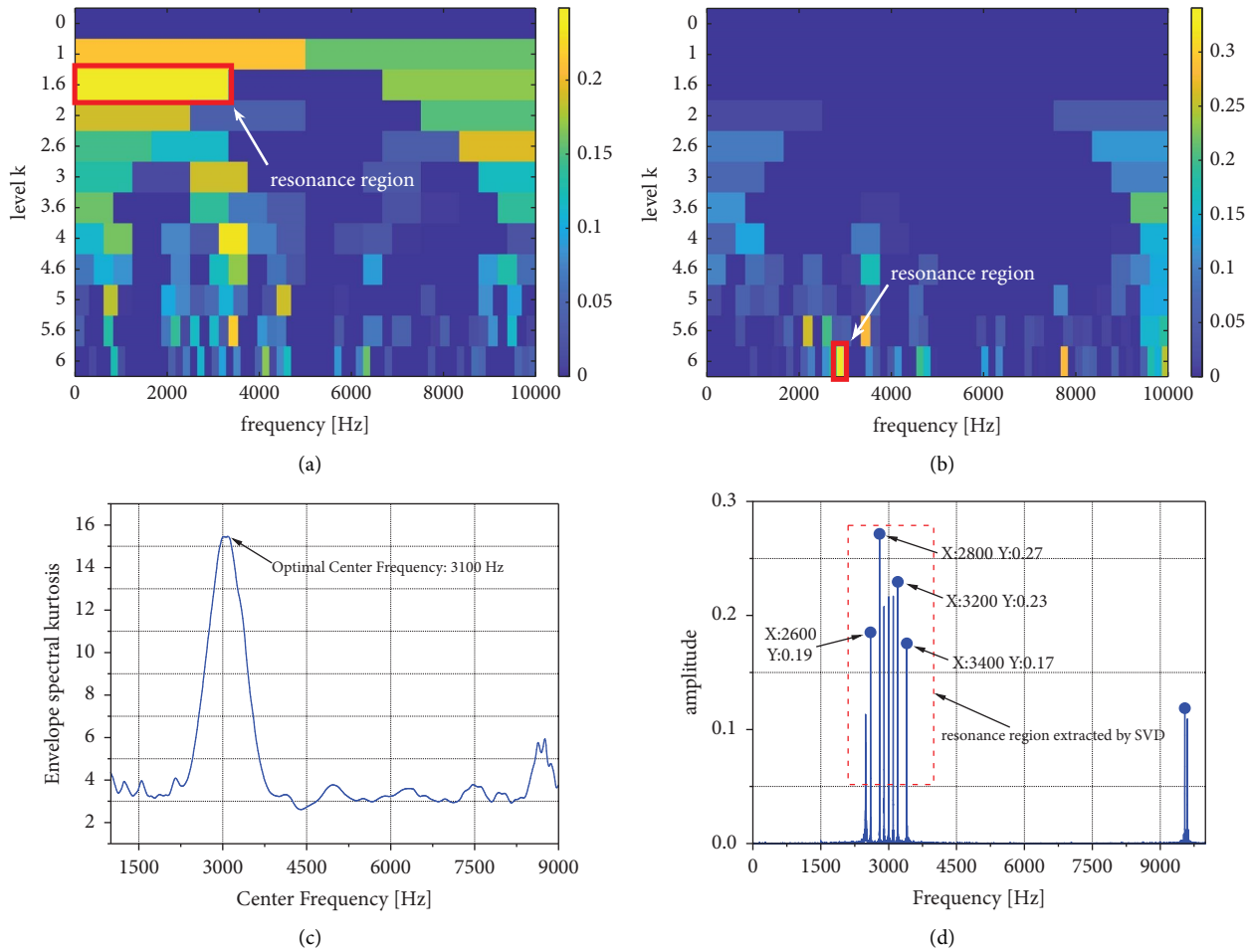

Figure 6: The comparison among FK, HTMFK, Protrugram, and SVD with simulation. (a) FK, $f_c = 3333.33$ Hz, $B_w = 1666.67$ Hz. (b) HTMFK, $f_c = 2890.625$ Hz·Hz, $B_w = 156.25$ Hz. (c) Protrugram, $f_c = 3100$ Hz, $B_w = 800$ Hz. (d) Spectrum of reconstructed signal by SVD.

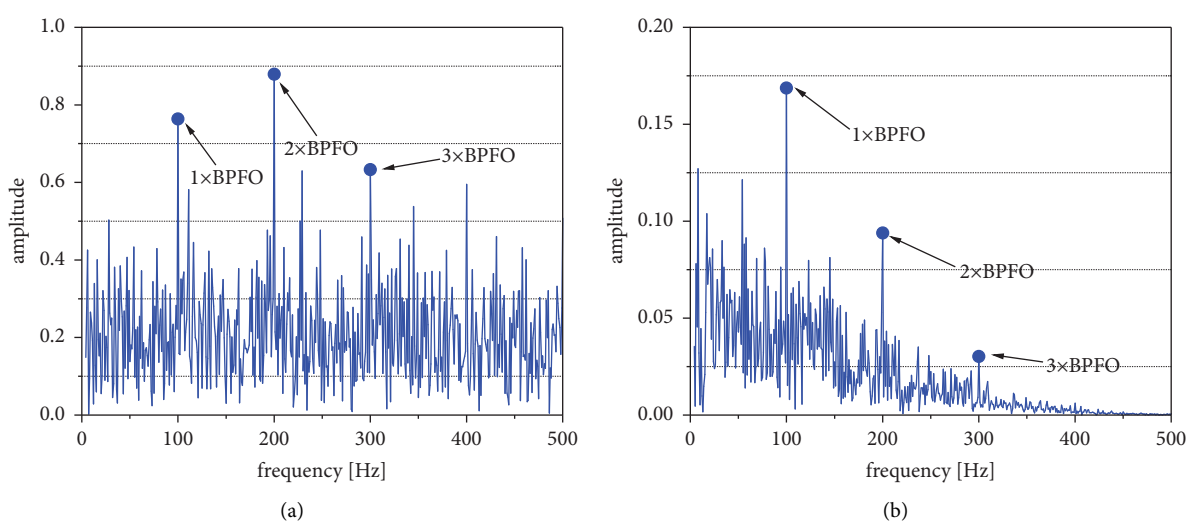

Figure 7: Continued.

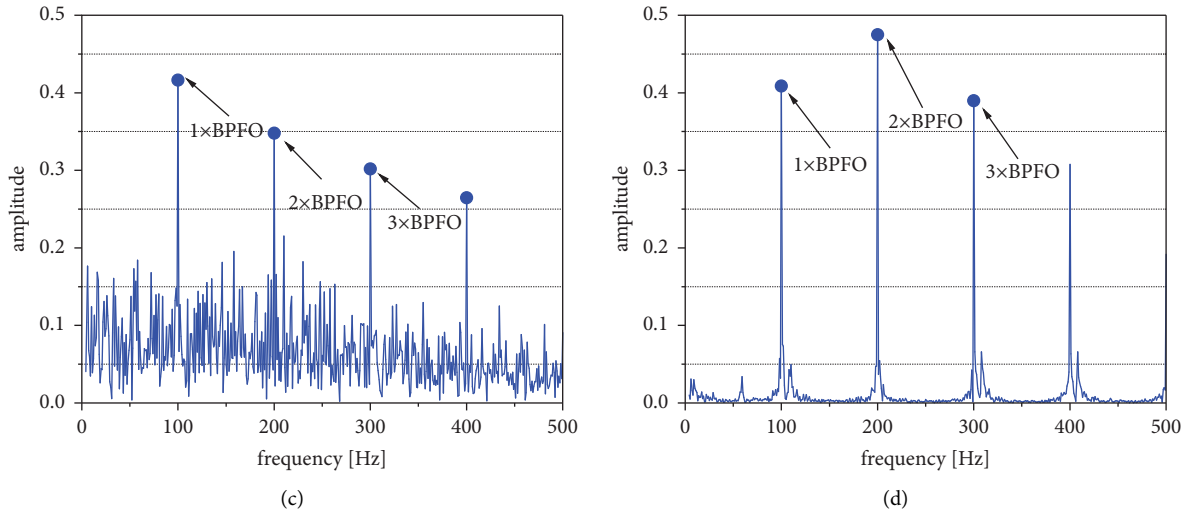

Figure 7: The SES among FK, HTMFK, Protrugram, and SVD with simulation. (a) FK. (b) HTMFK. (c) Protrugram. (d) SVD.

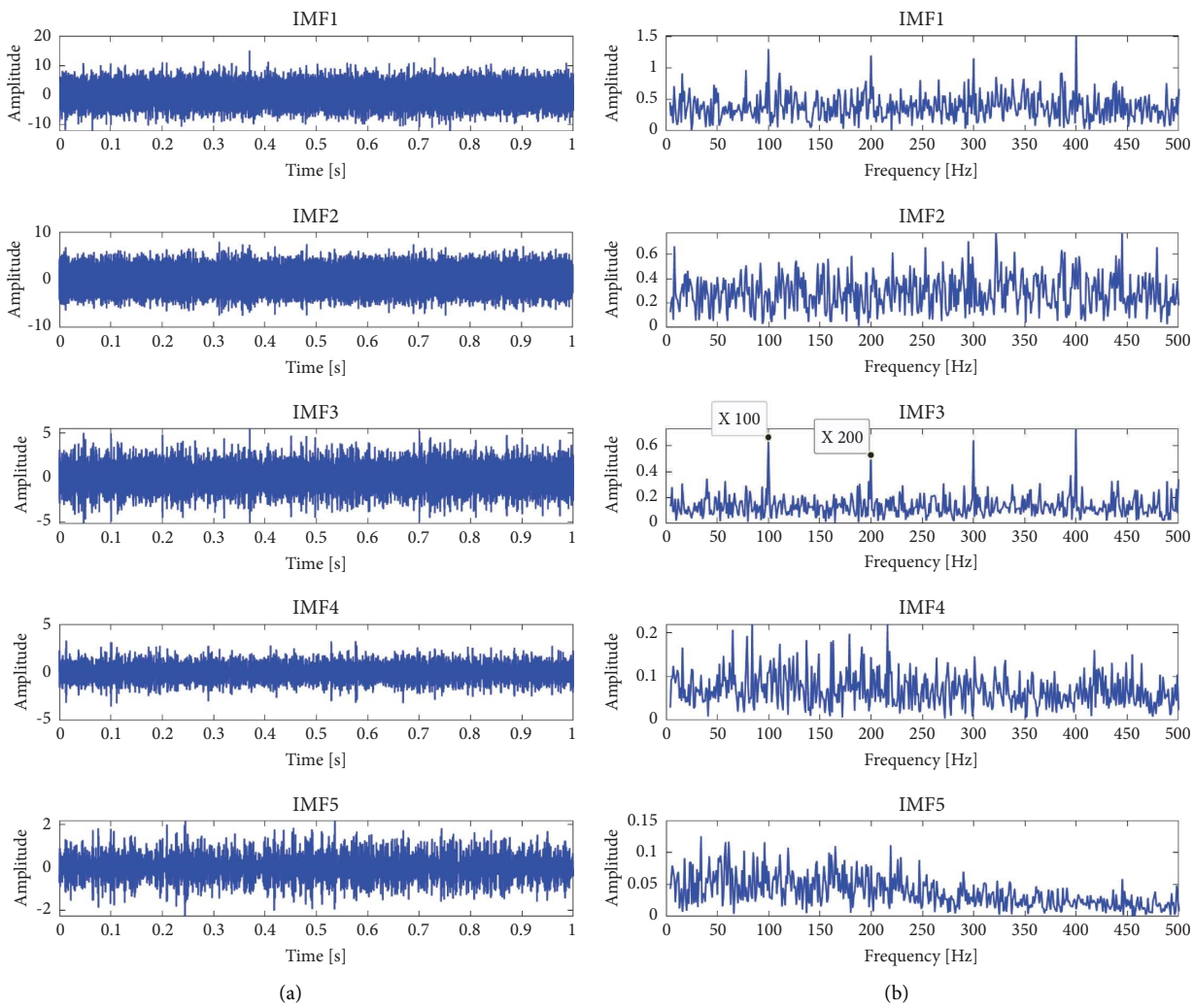

Figure 8: EEMD with simulation. (a) Temporal waveform. (b) SES.

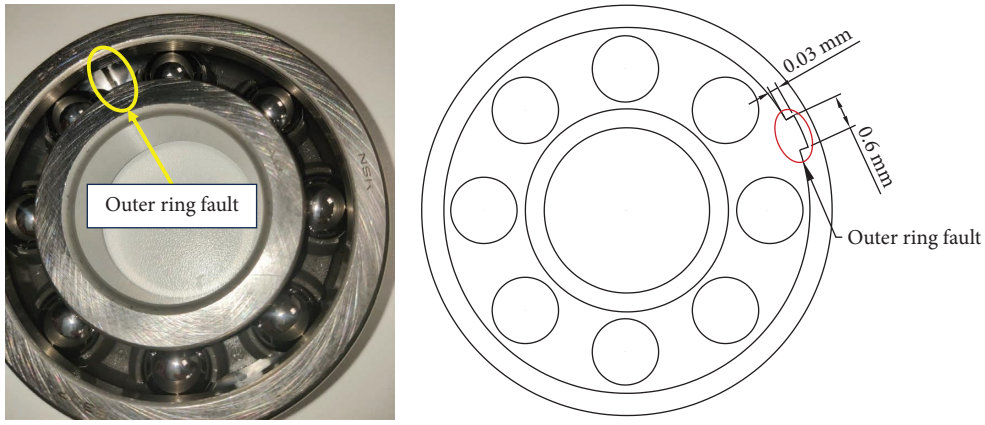

(a) (b)

Figure 9: The rolling bearing with specific fault information. (a) Actual photo of the bearing fault. (b) The artificial fault size.

Table 2: Parameters of rolling bearing.

Inner diameter (mm)	Outer diameter (mm)	Thickness (mm)	Rolling element diameter (mm)	Contact angle (°)	Number of rolling elements
35	80	21	13.494	0	8

Table 3: Operating conditions and states.

Serial number	High shaft speed (rpm)	Duration (s)	Motor torque (N·m)	Fault frequency
1	2000	10	50	102.04 Hz
2	3000	10	50	153.06 Hz
3	2000	10	20	102.04 Hz
4	3000	10	20	153.06 Hz
5	$0 \longrightarrow 5000 \longrightarrow 0$	60	50	None

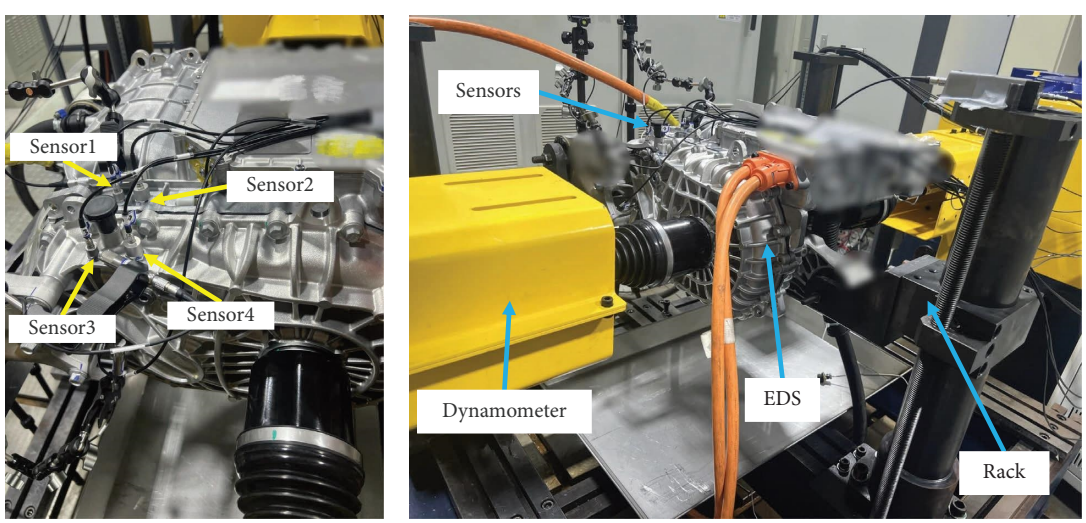

(a) (b)

Figure 10: Bench test system of EDS. (a) Sensor layout diagram. (b) EDS bench test system.

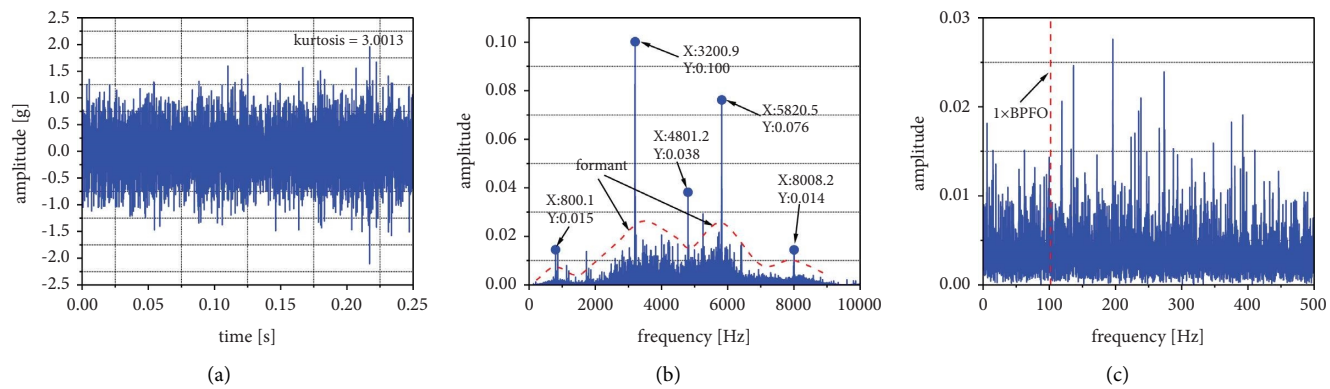

Figure 11: Experimental signal of EDS under 2000 rpm and 50 N·m. (a) Temporal waveform. (b) Spectrum. (c) Envelope spectrum.

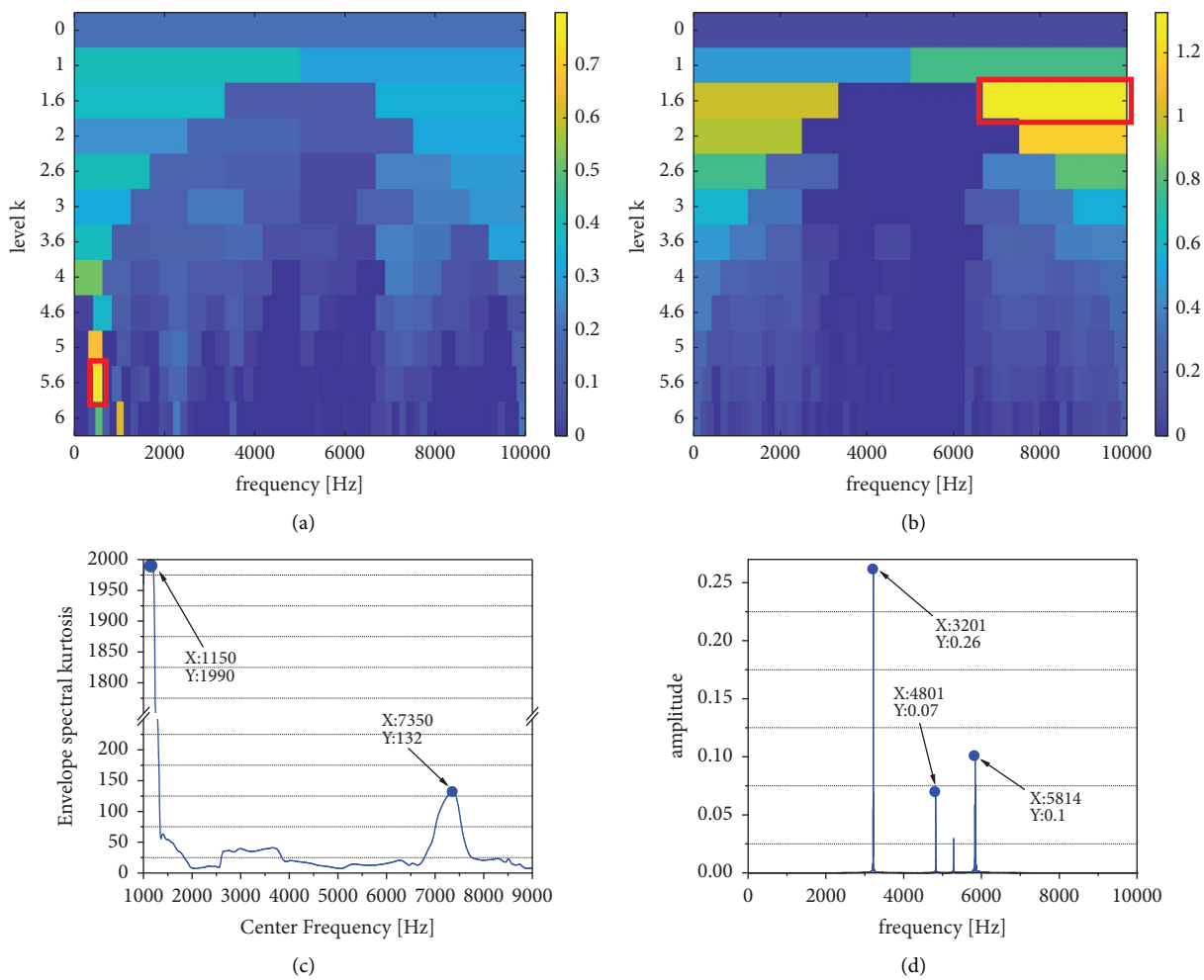

Figure 12: The comparison among FK, HTMFK, Protrugram, and SVD under 2000 rpm and 50 N·m. (a) FK, $f_c = 520.83$ Hz, $B_w = 208.33$ Hz. (b) HTMFK, $f_c = 8333.33$ Hz, $B_w = 3333.33$ Hz. (c) Protrugram, $f_c = 1150$ Hz, $B_w = 800$ Hz. (d) Spectrum of reconstructed signal by SVD.

Protrugram also identified an extreme value at 7350 Hz, which similar to the HTMFK result. From Figure 12(d), SVD still exhibits strong noise reduction ability, and the reconstructed signal spectrum mainly extracts the components of the original signal at 3201 Hz and 5814 Hz.

Figure 13 shows the SES of the filtered signal and reconstructed signal separately. Comparing the characteristic frequency of outer ring faults (BPFO), FK has completely failed which is shown in Figure 13(a). From Figure 13(b), HTMFK has obvious fault characteristics in SES, and the fault frequency

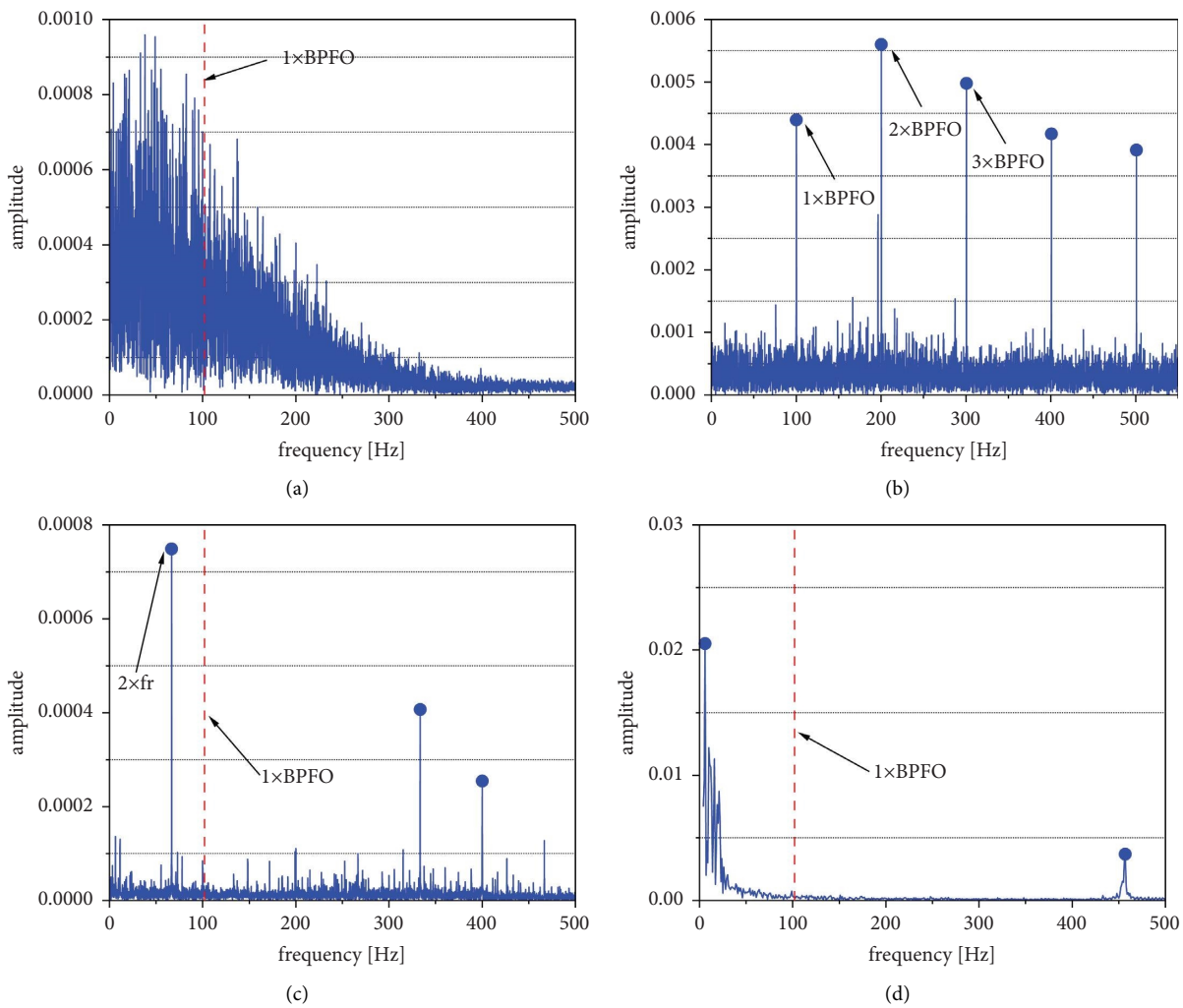

Figure 13: SES of FK, HTMFK, Protrugram, and SVD under 2000 rpm and 50 N·m. (a) FK. (b) HTMFK. (c) Protrugram. (d) SVD.

is similar to the theoretical value of 102 Hz. The main component extracted by the SES of Protrugram is the second-order rotational frequency (f_r) from Figure 13(c). However, SVD extract fault components incorrect which is shown in Figure 13(d). As mentioned in the simulation experiment, although SVD has strong noise reduction ability, the prerequisite is to find an effective resonance region. From Figure 14, EEMD ineffectual realize effective mode separation, and only second-order harmonic of rotational frequency can be observed in the SES of IMF4 and IMF5. By comparison, it can be seen that only HTMFK locates the resonance frequency band of bearing faults accurately and diagnoses the faults successfully.

The diagnosis results from the steady-state condition of 3000 rpm & 50 N·m are shown in Figures 15–18, which are similar to the condition of 2000 rpm & 50 N·m. From Figure 15, the fault impact is also obscured by noise. As shown in Figure 16, HTMFK still locates the resonance frequency band at a high frequency range above 7000 Hz, which similar to the extreme value at 7350 Hz of Protrugram. From Figure 17, HTMFK has more obvious fault characteristics which are similar to the theoretical calculation of 153 Hz. From Figure 18, SES of IMF5 extracted by EEMD has significant amplitude at 150.1 Hz. However, the amplitude of the second-order harmonic is too weak to determine the fault.

5.2. Accuracy Identification of HTMFK. According to the fault identification results of the above two operating conditions, the bearing fault has well diagnosed when the fault resonance frequency band is above 7000 Hz. Fault band identification under variable speed conditions is used to further verify the accuracy of the proposed method. The time-frequency domain under the operating condition of 0–5000 rpm & 50 N·m is shown in Figure 19. There are three obvious resonance regions, and HTMFK locates at the resonance region near 8000 Hz.

In order to verifying the accuracy of the identified resonance frequency band for fault diagnosis, a high pass filter (HPF) of 7000 Hz is constructed. This step can replace the determination of bandpass filter parameters in the previous process. The diagnostic results are shown in Figures 20–23, respectively.

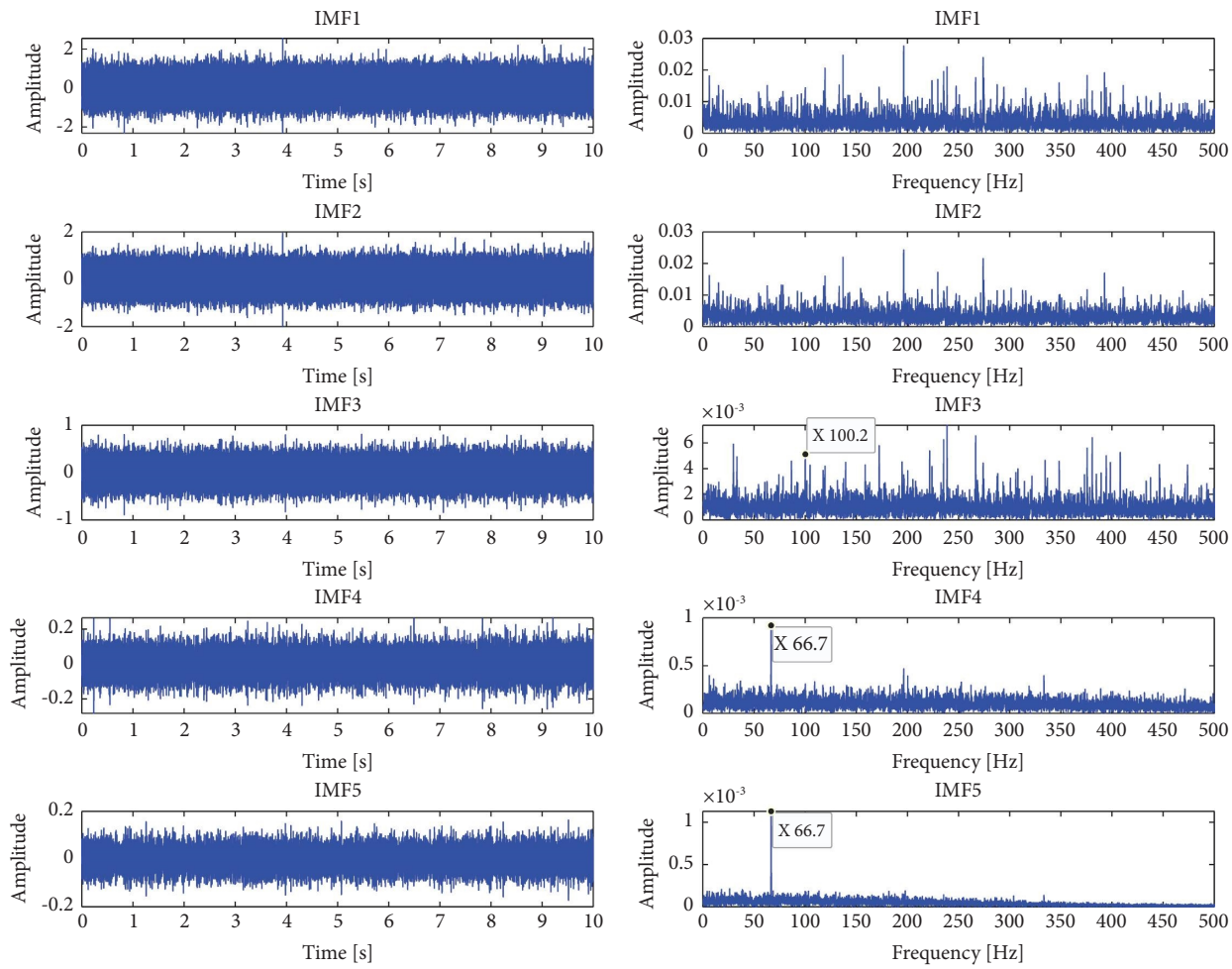

Figure 14: EEMD under 2000 rpm & 50 N·m.

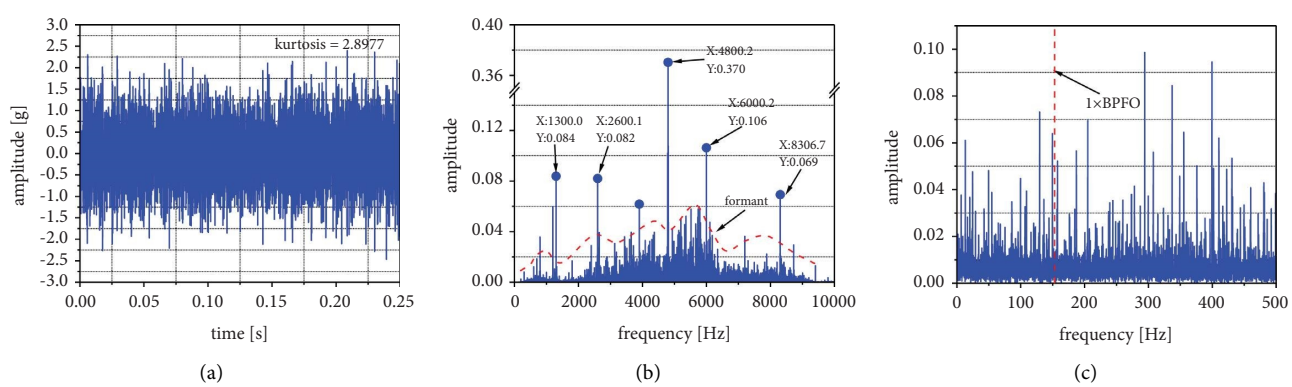

Figure 15: Experimental signal of EDS under 3000 rpm and 50 N·m. (a) Temporal waveform. (b) Spectrum. (c) Envelope spectrum.

For the working torque of 20 N·m, the SES of HPF has more obvious fault characteristics and provides effective diagnostic results. However, the SES of FK and Protrugram indicate that the resonance frequency bands located by these two methods are not accurate enough to diagnose bearing faults. SVD still extract bearing fault information ineffectively. The fault features extracted by EEMD are mainly second-order rotation frequency and has a certain effect under the working condition of 3000 rpm and 20 N·m. The above results indicate that the HPF based on HTMFK is effective and reliable.

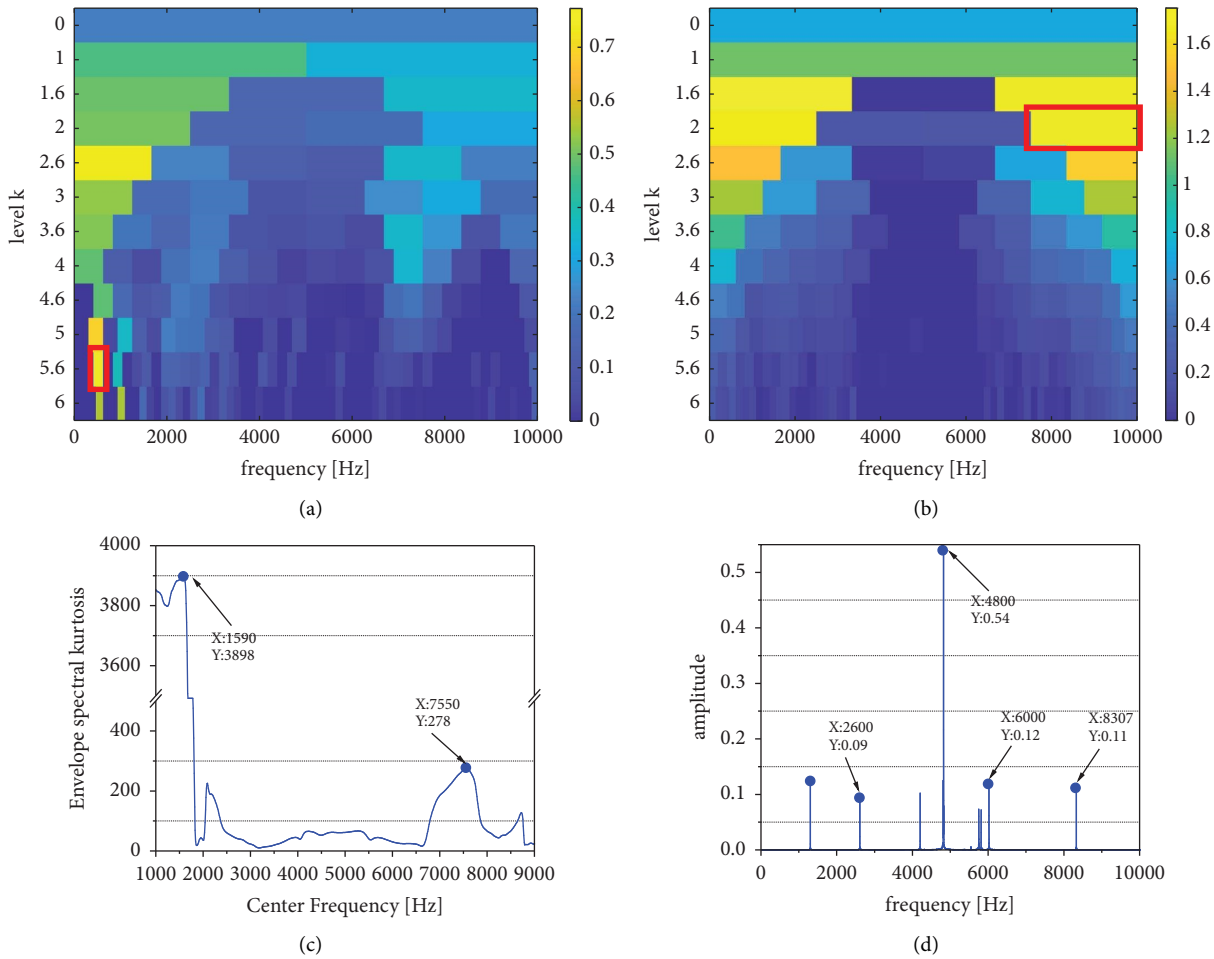

Figure 16: The comparison among FK, HTMFK, Protrugram, and SVD under 3000 rpm & 50 N·m. (a) FK, $f_c = 520.83$ Hz, $B_w = 208.33$ Hz. (b) HTMFK, $f_c = 8750$ Hz, $B_w = 2500$ Hz. (c) Protrugram, $f_c = 1590$ Hz, $B_w = 800$ Hz. (d) Spectrum of reconstructed signal by SVD.

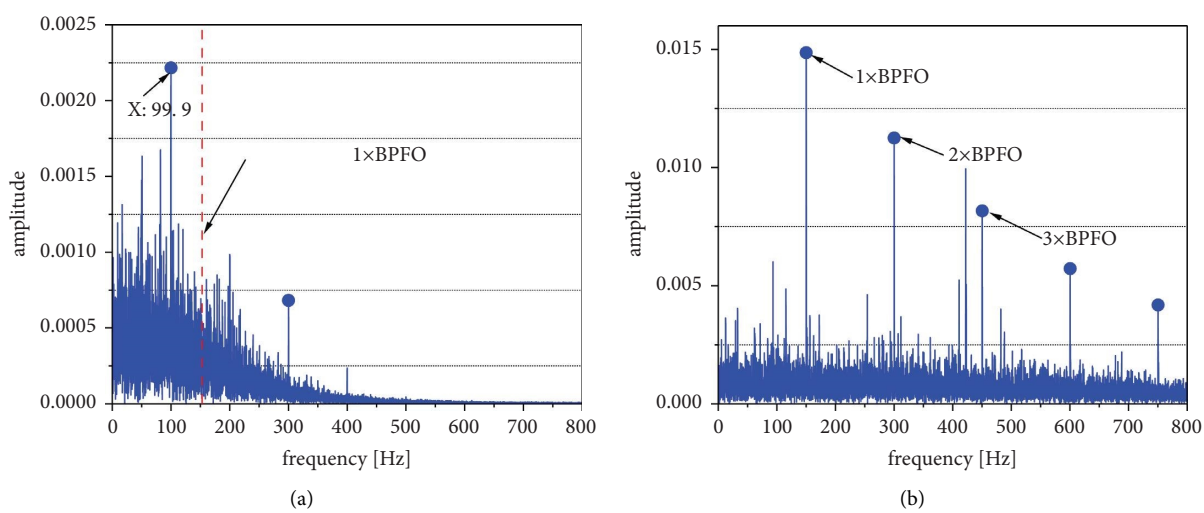

Figure 17: Continued.

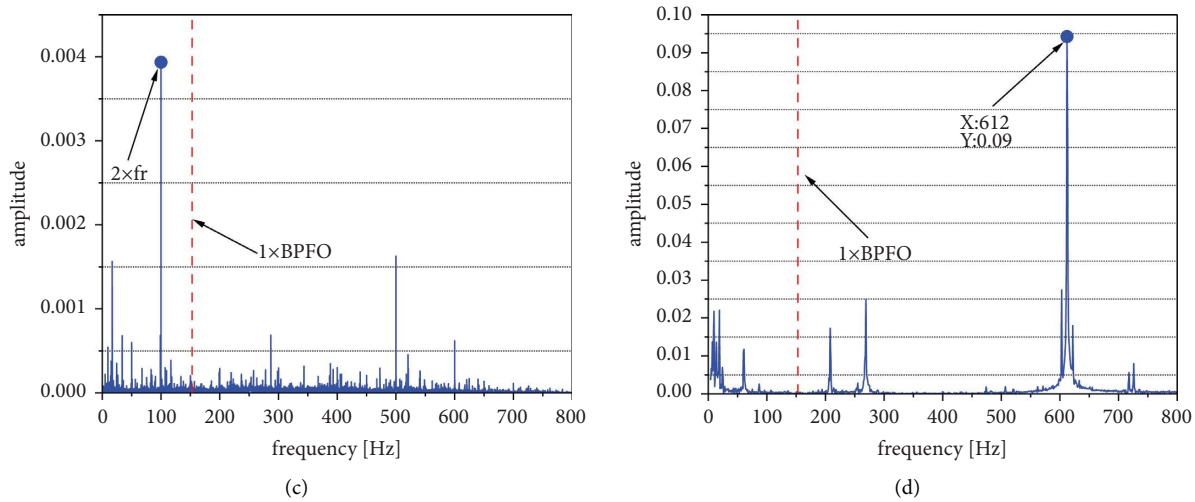

Figure 17: SES of FK, HTMFK, Protrugram, and SVD under 3000 rpm and 50 N·m. (a) FK. (b) HTMFK. (c) Protrugram. (d) SVD.

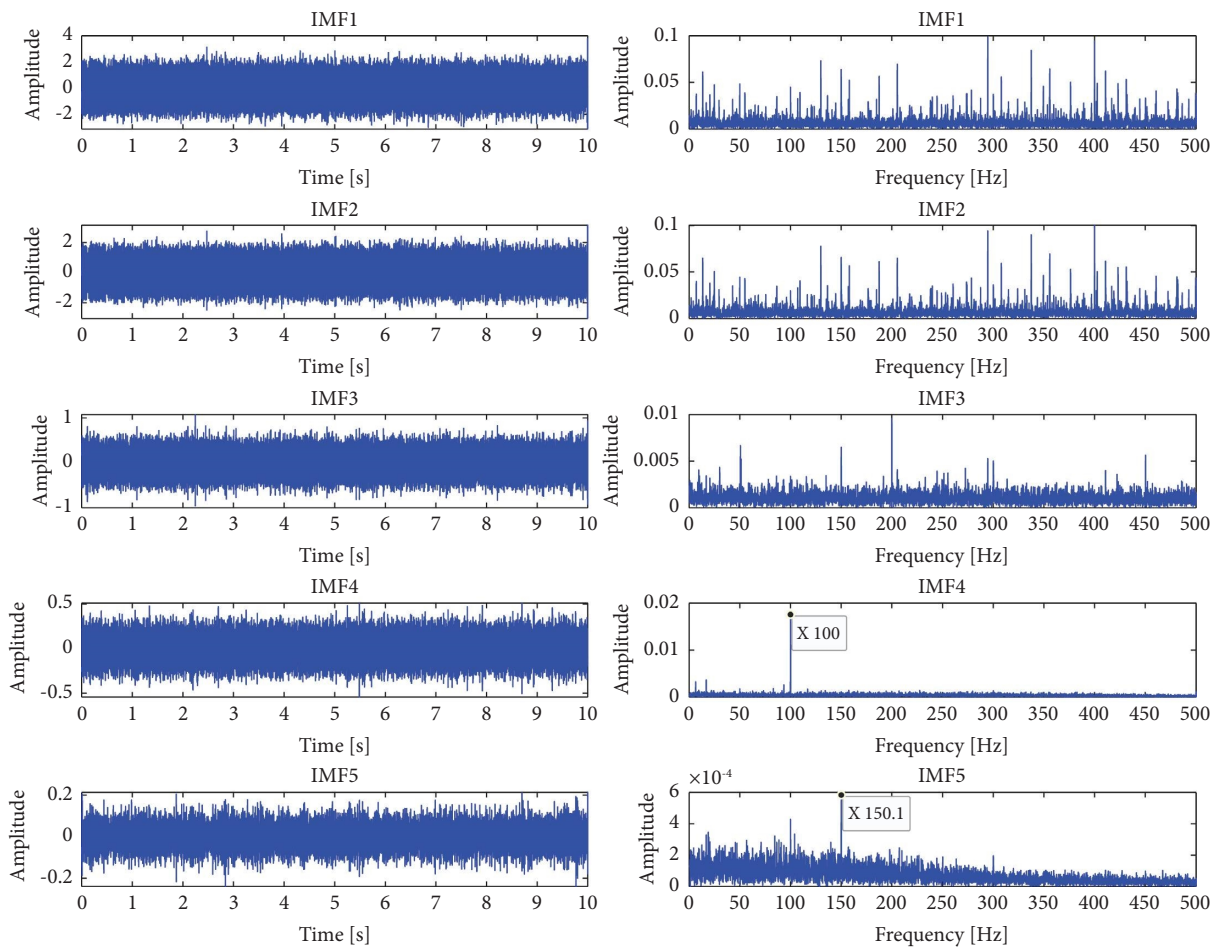

Figure 18: EEMD under 3000 rpm and 50 N·m.

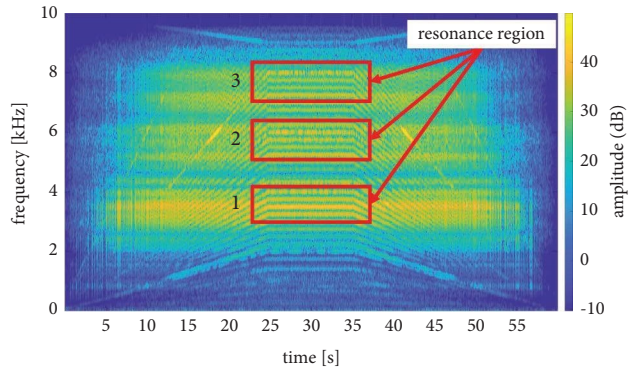

Figure 19: Time-frequency domain under 0–5000 rpm and 50 N·m.

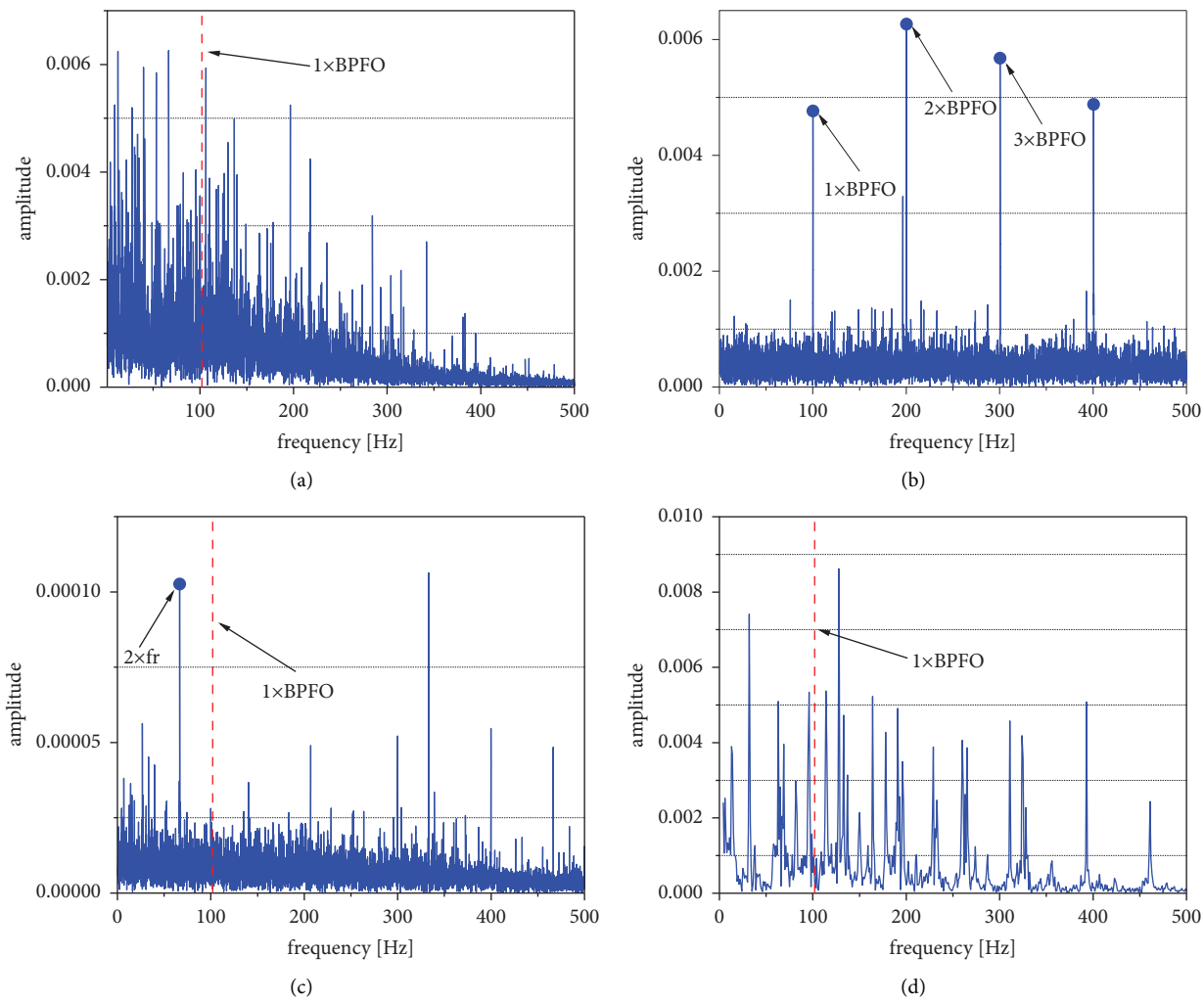

Figure 20: SES of FK, HTMFK, Protrugram and SVD under 2000 rpm and 20 N·m. (a) FK, $f_c = 2968.75$ Hz, $B_w = 312.5$ Hz. (b) HPF of 7000 Hz. (c) Protrugram, $f_c = 1300$ Hz, $B_w = 800$ Hz. (d) SVD.

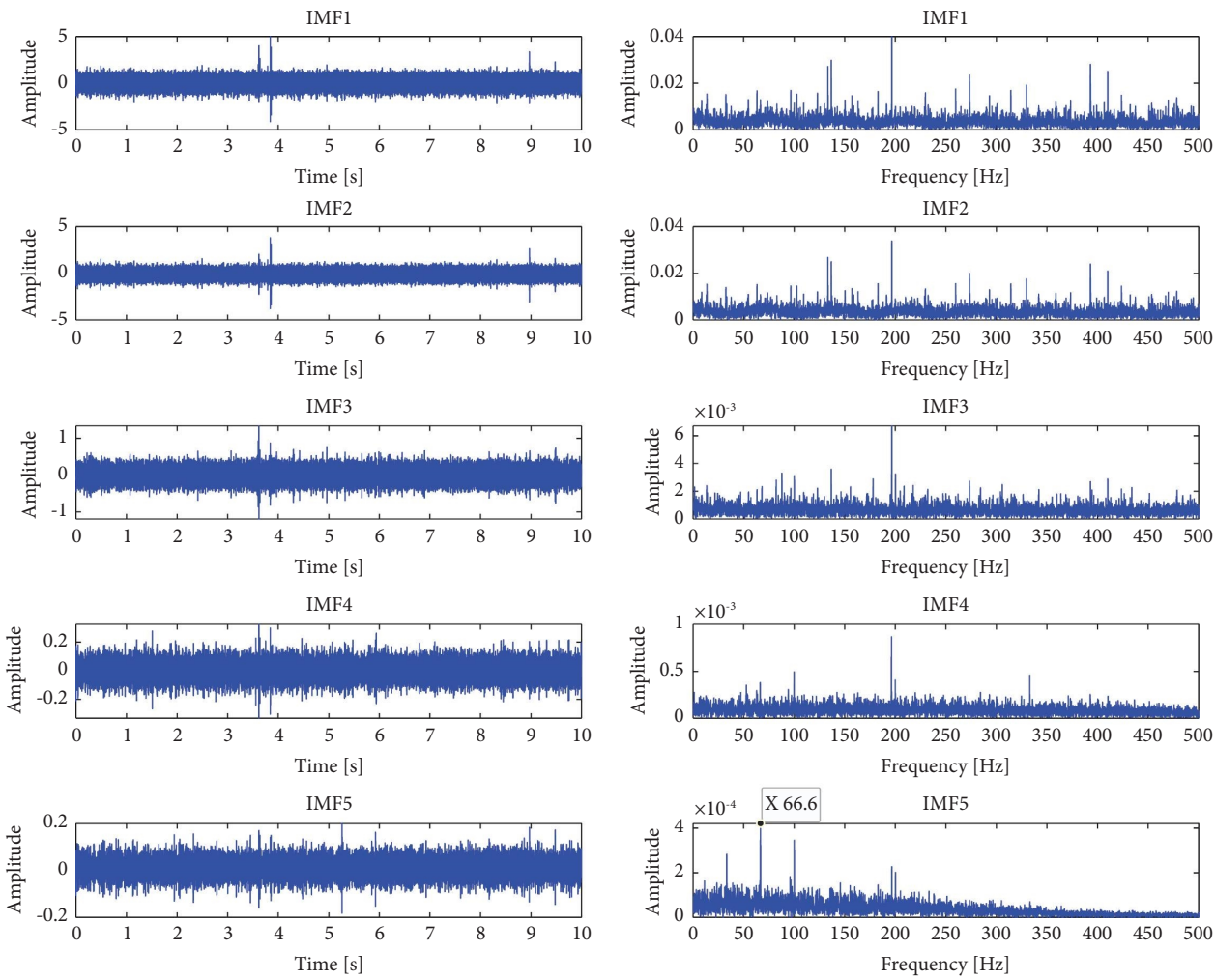

Figure 21: EEMD under 2000 rpm and 20 N·m.

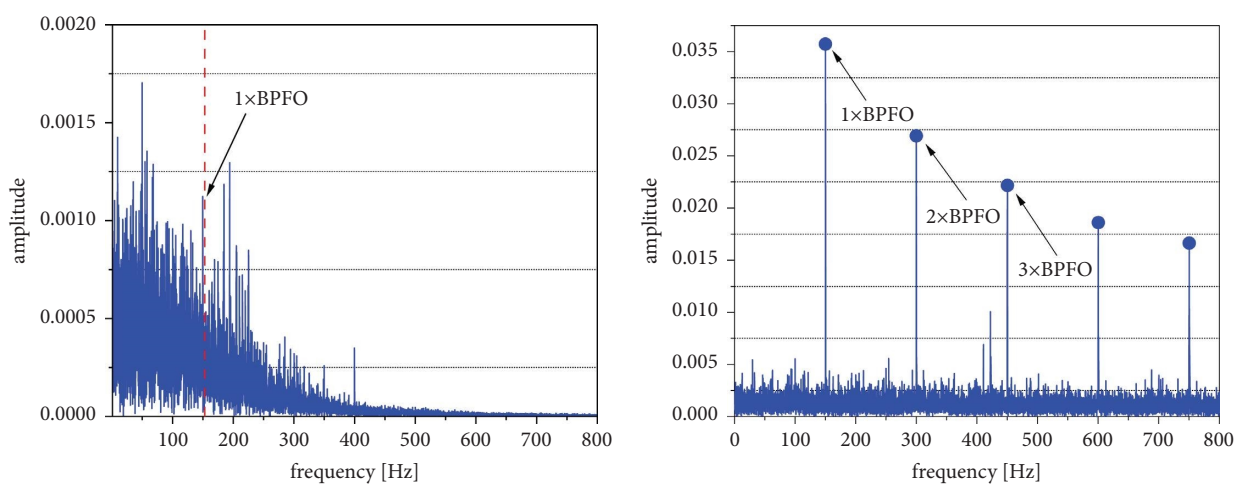

(a) (b)

Figure 22: Continued.

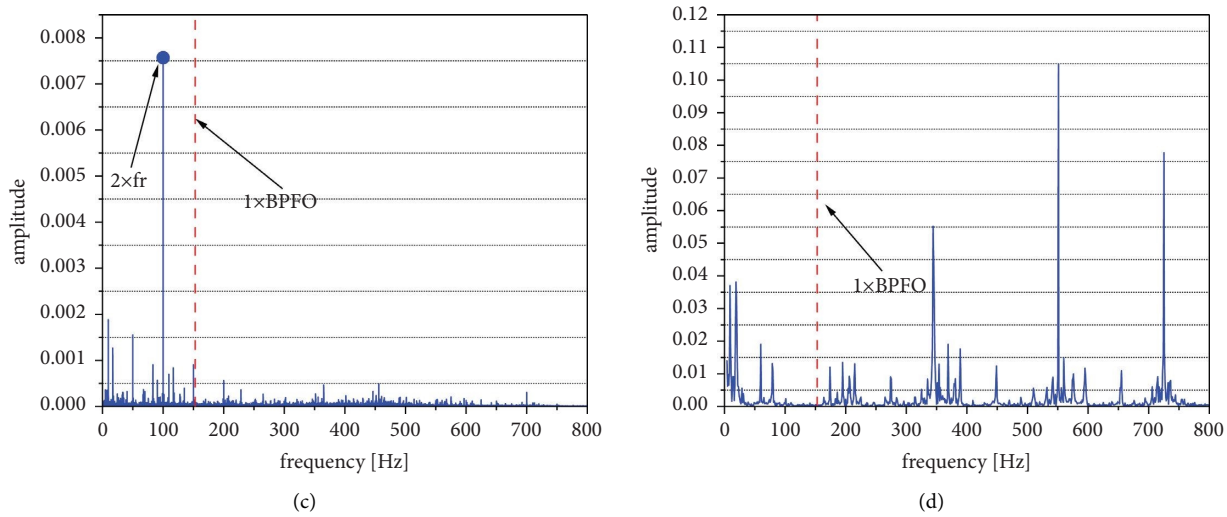

Figure 22: SES of FK, HTMFK, Protrugram, and SVD under 3000 rpm & 20 N·m. (a) FK, $f_c = 520.83$ Hz, $B_w = 208.33$ Hz. (b) HPF of 7000 Hz. (c) Protrugram, $f_c = 1000$ Hz, $B_w = 800$ Hz. (d) SVD.

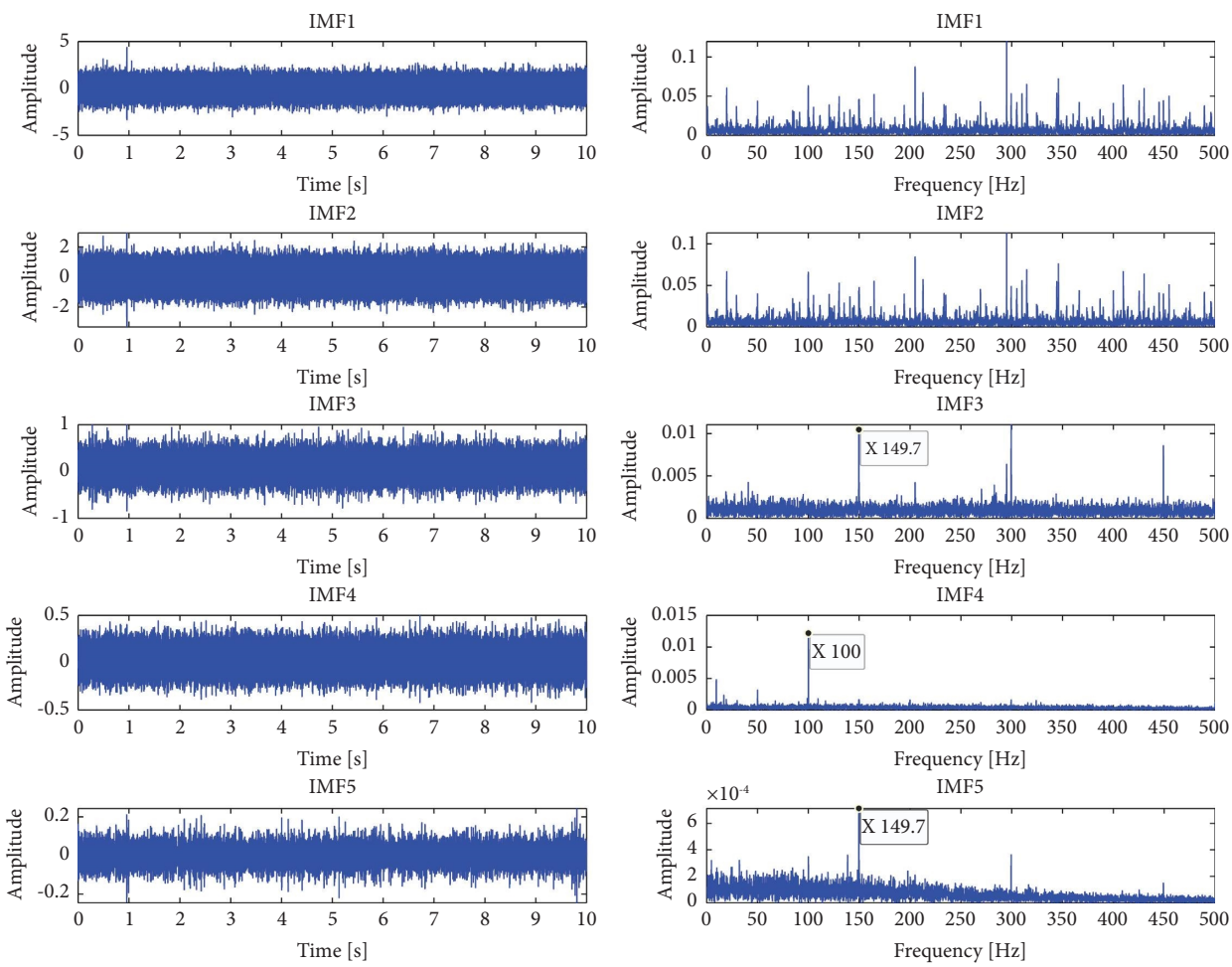

Figure 23: EEMD under 3000 rpm and 20 N·m.

6. Conclusion

A novel method is established as HTMFK for detecting the resonance frequency band of weak bearing faults of EDS. The effectiveness of proposed method has been verified through simulation signals and bench fault test data of EDS. Meanwhile, by comparing the results of HTMFK with other methods, the superiority of HTMFK is demonstrated. The following conclusions are drawn in this article:

(1) Demodulation of fault signals based on Hilbert envelope can effectively amplify the weak fault information of bearing outer ring.

(2) From the simulation results, the center frequency obtained by HTMFK is closer to the theoretical value than FK. The resonance frequency band located is more reliable.

(3) Bench test of rolling bearing fault in EDS is conducted. Compared with SES of FK and other methods, the accuracy and effectiveness of detected resonance frequency bands from weak outer ring fault of EDS are verified.

(4) The results of variable speed operating conditions and the diagnostic results of HPF for 20 N·m operating conditions indicate that the resonance frequency band located by HTMFK is effective and accurate. HTMFK is effective for fault diagnosis of weak bearing faults in EDS.

Data Availability

The data that support the findings of this study are available from the corresponding author upon reasonable request.

Conflicts of Interest

The authors declare that they have no conflicts of interest.

Acknowledgments

This work was supported by NIO University Programme (NIO UP, Grant No. 3010030813) and the National Natural Science Foundation of China (Grant No. 52301328). The authors would like to gratefully acknowledge NIO for their support.

References

[1] M. S. Hossain, L. Kumar, M. M. Islam, and J. Selvaraj, "A comprehensive review on the integration of electric vehicles for sustainable development," *Journal of Advanced Transportation*, vol. 2022, Article ID 3868388, 26 pages, 2022/10/11 2022.

[2] T. Mo, Y. Li, K.-T. Lau, C. K. Poon, Y. Wu, and Y. Luo, "Trends and emerging technologies for the development of electric vehicles," *Energies*, vol. 15, no. 17, p. 6271, 2022.

[3] B. E. Lebrouhi, Y. Khattari, B. Lamrani, M. Maaroufi, Y. Zeraouli, and T. Kousksou, "Key challenges for a large-scale development of battery electric vehicles: a comprehensive review," *Journal of Energy Storage*, vol. 44, Article ID 103273, 2021.

[4] X. Wang, S. Lu, K. Chen, Q. Wang, and S. Zhang, "Bearing Fault diagnosis of switched reluctance motor in electric vehicle powertrain via multisensor data fusion," *IEEE Transactions on Industrial Informatics*, vol. 18, no. 4, pp. 2452–2464, 2022.

[5] F. He, G. Xie, and J. Luo, "Electrical bearing failures in electric vehicles," *Friction*, vol. 8, no. 1, pp. 4–28, 2020/02/01 2020.

[6] Z. Xiao, M. Hu, S. Chen, and K. Cao, "Bearing electrical-erosion damage in electrical drive systems: a review," *IEEE Transactions on Transportation Electrification*, p. 1, 2024.

[7] M. Buzzoni, G. D'Elia, and M. Cocconcelli, "A tool for validating and benchmarking signal processing techniques applied to machine diagnosis," *Mechanical Systems and Signal Processing*, vol. 139, Article ID 106618, 2020.

[8] M. K. Babouri, N. Ouelaa, T. Kebabsa, and A. Djebala, "Application of the cyclostationarity analysis in the detection of mechanical defects: comparative study," *The International Journal of Advanced Manufacturing Technology*, vol. 103, no. 5-8, pp. 1681–1699, 2019/08/01 2019.

[9] M. Yu, M. Fang, W. Chen, and H. Cong, "Compound faults feature extraction of inter-shaft bearing based on vibration signal of whole aero-engine," *Journal of Vibration and Control*, vol. 29, no. 1-2, pp. 51–64, 2023.

[10] N. E. Huang, Z. Shen, S. R. Long et al., "The empirical mode decomposition and the Hilbert spectrum for nonlinear and non-stationary time series analysis," *Proceedings of the Royal Society of London Series A: Mathematical, Physical and Engineering Sciences*, vol. 454, no. 1971, pp. 903–995, 1998.

[11] D. Meng, H. Wang, S. Yang, Z. Lv, Z. Hu, and Z. Wang, "Fault analysis of wind power rolling bearing based on EMD feature extraction," *Computer Modeling in Engineering and Sciences*, vol. 130, no. 1, pp. 543–558, 2022.

[12] Y. Sun, S. Li, and X. J. M. Wang, "Bearing fault diagnosis based on EMD and improved Chebyshev distance in SDP image," *Measurement*, vol. 176, no. 17, Article ID 109100, 2021.

[13] L. Jia, H. Wang, L. Jiang, and W. Du, "Weak fault detection of rolling element bearing combining robust EMD with adaptive maximum second-order cyclostationarity blind deconvolution," *Journal of Vibration and Control*, vol. 29, no. 9-10, pp. 2374–2391, 2023.

[14] Z. Wu and N. E. Huang, "Ensemble empirical mode decomposition: a noise-assisted data analysis method," *Advances in Adaptive Data Analysis*, vol. 01, no. 01, pp. 1–41, 2009.

[15] F. Liu, J. Gao, and H. Liu, "The feature extraction and diagnosis of rolling bearing based on CEEMD and LDWPSO-PNN," *IEEE Access*, vol. 8, pp. 19810–19819, 2020.

[16] F. Liu, J. Gao, and H. Liu, "a fault diagnosis solution of rolling bearing based on MEEMD and QPSO-LSSVM," *IEEE Access*, vol. 8, pp. 101476–101488, 2020.

[17] K. Dragomiretskiy and D. Zosso, "Variational mode decomposition," *IEEE Transactions on Signal Processing*, vol. 62, no. 3, pp. 531–544, 2014.

[18] Z. Jin, D. Chen, D. He, Y. Sun, and X. Yin, "Bearing Fault diagnosis based on VMD and improved CNN," *Journal of Failure Analysis and Prevention*, vol. 23, no. 1, pp. 165–175, 2023.

[19] J. Gu, Y. Peng, H. Lu et al., "An optimized variational mode decomposition method and its application in vibration signal analysis of bearings," *Structural Health Monitoring*, vol. 21, no. 5, pp. 2386–2407, 2022.

[20] Z. Jin, D. He, and Z. Wei, "Intelligent fault diagnosis of train axle box bearing based on parameter optimization VMD and improved DBN," *Engineering Applications of Artificial Intelligence*, vol. 110, Article ID 104713, 2022.

[21] H. Li, T. Liu, X. Wu, and S. Li, "Correlated SVD and its application in bearing fault diagnosis," *IEEE Transactions on Neural Networks and Learning Systems*, vol. 34, no. 1, pp. 355–365, 2023.

[22] H. Zhu, Z. He, Y. Xiao, J. Wang, and H. Zhou, "Bearing Fault diagnosis method based on improved singular value decomposition package," *Sensors*, vol. 23, pp. 3759–3767, 2023.

[23] J. Gilles, "Empirical wavelet transform," *IEEE Transactions on Signal Processing*, vol. 61, no. 16, pp. 3999–4010, 2013.

[24] H. Yu, H. Li, and Y. Li, "Vibration signal fusion using improved empirical wavelet transform and variance contribution rate for weak fault detection of hydraulic pumps," *ISA Transactions*, vol. 107, pp. 385–401, 2020.

[25] M. Hu, G. Wang, and K. Ma, "Identification of wind turbine gearbox weak compound fault based on optimal empirical wavelet transform," *Measurement Science and Technology*, vol. 34, no. 4, Article ID 045003, 2023.

[26] J. Xue, H. Xu, X. Liu, D. Zhang, and Y. Xu, "Application of enhanced empirical wavelet transform and correlation kurtosis in bearing fault diagnosis," *Measurement Science and Technology*, vol. 34, no. 3, Article ID 035023,, 2023.

[27] R. Dwyer, "Use of the kurtosis statistic in the frequency domain as an aid in detecting random signals," *IEEE Journal of Oceanic Engineering*, vol. 9, no. 2, pp. 85–92, 1984.

[28] J. Antoni and R. B. Randall, "The spectral kurtosis: application to the vibratory surveillance and diagnostics of rotating machines," *Mechanical Systems and Signal Processing*, vol. 2, p. 20, 2006.

[29] J. Antoni, "Fast computation of the kurtogram for the detection of transient faults," *Mechanical Systems and Signal Processing*, vol. 21, no. 1, pp. 108–124, 2007.

[30] J. Antoni, "The spectral kurtosis: a useful tool for characterising non-stationary signals," *Mechanical Systems and Signal Processing*, vol. 20, no. 2, pp. 282–307, 2006.

[31] H. Ma, J. Wang, B. Han et al., "Nonlinear fast kurtogram for the extraction of gear fault features with shock interference," *Measurement Science and Technology*, vol. 34, no. 2, Article ID 024001, 2022/11/02 2023.

[32] K. Liang, M. Zhao, J. Lin, C. Ding, J. Jiao, and Z. Zhang, "A novel indicator to improve fast kurtogram for the health monitoring of rolling bearing," *IEEE Sensors Journal*, vol. 20, no. 20, pp. 12252–12261, 2020.

[33] C. Liu, X. Gao, D. Chi, Y. He, M. Liang, and H. Wang, "Online chatter detection in milling using fast kurtogram and frequency band power," *European Journal of Mechanics- A: Solids*, vol. 90, Article ID 104341, 2021.

[34] J. Yao, J. Zhao, Y. Deng, and R. Langari, "Weak Fault feature extraction of rotating machinery based on double-window spectrum fusion enhancement," *IEEE Transactions on Instrumentation and Measurement*, vol. 69, no. 4, pp. 1029–1040, 2020.

[35] W. Song, L. Guo, A. Duan et al., "Multispectral balanced automatic fault diagnosis for rolling bearings under variable speed conditions," *Structural Control and Health Monitoring*, vol. 2023, Article ID 9369850, 17 pages, 2023.

[36] B. Chen, W. Zhang, J. Xi Gu et al., "Product envelope spectrum optimization-gram: an enhanced envelope analysis for rolling bearing fault diagnosis," *Mechanical Systems and Signal Processing*, vol. 193, Article ID 110270, 2023.

[37] J. Meng, C. Yan, T. Wen, and Z. Wang, "Identification of initial fault time for bearing based on monitoring indicator, WEMD and Infogram," *Journal of Vibroengineering*, vol. 24, no. 7, pp. 1291–1312, 2022.

[38] B. Li, X. Xu, H. Tan, P. Shi, and Z. Qiao, "Cyclogram: an effective method for selecting frequency bands for fault diagnosis of rolling element bearings," *Measurement Science and Technology*, vol. 34, no. 9, Article ID 094003, 2023/06/07 2023.